

Detecting the relativistic galaxy bispectrum

Roy Maartens^{1,2}, Sheean Jolicoeur¹, Obinna Umeh²,
Eline M. De Weerd³, Chris Clarkson^{3,1,4}, Stefano Camera^{5,6,1}

¹Department of Physics & Astronomy, University of the Western Cape, Cape Town 7535, South Africa

²Institute of Cosmology & Gravitation, University of Portsmouth, Portsmouth PO1 3FX, UK

³School of Physics & Astronomy, Queen Mary University of London, London E1 4NS, UK

⁴Department of Mathematics & Applied Mathematics, University of Cape Town, Cape Town 7701, South Africa

⁵Dipartimento di Fisica, Università degli Studi di Torino, 10125 Torino, Italy

⁶Istituto Nazionale di Fisica Nucleare, Sezione di Torino, 10125 Torino, Italy

Abstract. The Fourier galaxy bispectrum is complex, with the imaginary part arising from leading-order relativistic corrections, due to Doppler, gravitational redshift and related line-of-sight effects in redshift space. The detection of the imaginary part of the bispectrum is potentially a smoking gun signal of relativistic contributions. We investigate whether next-generation spectroscopic surveys could make such a detection. For a Stage IV spectroscopic $H\alpha$ survey similar to Euclid, we find that the cumulative signal to noise of this relativistic signature is $\mathcal{O}(10)$. Long-mode relativistic effects couple to short-mode Newtonian effects in the galaxy bispectrum, but not in the galaxy power spectrum. This is the basis for detectability of relativistic effects in the bispectrum of a single galaxy survey, whereas the power spectrum requires multiple galaxy surveys to detect the corresponding signal.

Contents

1	INTRODUCTION	1
2	SIGNAL TO NOISE	4
2.1	Relativistic contribution to the variance	5
2.2	Nonlinear effects	5
2.3	Summations over triangles	6
3	GALAXY SURVEY	6
3.1	Evolution bias and magnification bias	7
3.2	Signal to noise of the relativistic bispectrum	9
3.3	Including cosmological parameters	12
4	CONCLUSIONS	13
A	APPENDIX	15

1 INTRODUCTION

The bispectrum of number count fluctuations in redshift space will become an increasingly important complement to the power spectrum in the extraction of cosmological information from galaxy surveys, in the measurement of clustering bias parameters and in the breaking of degeneracies between the clustering amplitude and growth rate. Analysis of the Fourier galaxy bispectrum is already well advanced for existing survey data (e.g [1, 2]) and for mock data of future surveys (e.g. [3–6]).

Here we highlight a feature of the tree-level Fourier galaxy bispectrum which follows from the leading-order relativistic contribution – due to Doppler, gravitational redshift and related line-of-sight effects – that is omitted in the standard Newtonian analysis. These effects generate an imaginary part of the galaxy bispectrum, which can be understood as follows (see also [7–9] for a more general discussion). The Doppler-type contributions to the galaxy density contrast involve one or three derivatives of scalars along the fixed line of sight \mathbf{n} [see (1.6), (1.7) below]. In Fourier space, with the plane-parallel approximation, we have $\mathbf{n} \cdot \nabla \rightarrow i \mathbf{n} \cdot \mathbf{k}$, and this leads to imaginary corrections to the galaxy density contrast, which do not cancel in the bispectrum, unlike in the power spectrum. At first order, we have $\delta_g = \delta_{gN} + \delta_{gD}$, where the Newtonian part δ_{gN} is real and scales as the linear matter density contrast δ . The relativistic Doppler-type part δ_{gD} scales as $i(\mathcal{H}/k)\delta$ (see [7, 8, 10, 11] and below). At second order, the relativistic contribution $\delta_{gD}^{(2)}$ scales as $i(\mathcal{H}/k)(\delta)^2$ (see [8] and below).

In the case of the galaxy auto-power spectrum, $P_g \sim \langle |\delta_g|^2 \rangle$, the relativistic part is real and scales as $(\mathcal{H}/k)^2 P$: therefore we can neglect P_{gD} at leading order. By contrast, for the galaxy bispectrum, $B_g \sim \langle \delta_g \delta_g \delta_g^{(2)} \rangle$, a coupling of relativistic contributions to short-scale Newtonian terms (which is absent in P_g) produces a B_{gD} that is imaginary and scales as $i(\mathcal{H}/k)P^2$. We therefore expect these relativistic effects to be more accessible in the bispectrum than in the power spectrum, for the case of a single tracer of the matter distribution.

Although the galaxy bispectrum is statistically isotropic, the plane-parallel approximation in redshift space breaks 3-dimensional isotropy, since a preferred direction is imposed by the observer's fixed line of sight.

Let us introduce a more explicit analysis, as follows.

At tree-level, the Fourier galaxy bispectrum at a redshift z is given by

$$\langle \delta_g(z, \mathbf{k}_1) \delta_g(z, \mathbf{k}_2) \delta_g^{(2)}(z, \mathbf{k}_3) \rangle + 2 \text{ cp} = 2(2\pi)^3 B_g(z, \mathbf{k}_1, \mathbf{k}_2, \mathbf{k}_3) \delta^{\text{Dirac}}(\mathbf{k}_1 + \mathbf{k}_2 + \mathbf{k}_3), \quad (1.1)$$

where cp denotes cyclic permutation and the factor 2 on the right arises from the convention that the total number density contrast is $\delta_g + \delta_g^{(2)}/2$. In terms of the first- and second-order kernels, we have

$$B_g(z, \mathbf{k}_1, \mathbf{k}_2, \mathbf{k}_3) = \mathcal{K}^{(1)}(z, \mathbf{k}_1) \mathcal{K}^{(1)}(z, \mathbf{k}_2) \mathcal{K}^{(2)}(z, \mathbf{k}_1, \mathbf{k}_2, \mathbf{k}_3) P(z, k_1) P(z, k_2) + 2 \text{ cp}, \quad (1.2)$$

where P is the linear matter power spectrum. The $9 - 3 = 6$ degrees of freedom in the triangle condition $\mathbf{k}_1 + \mathbf{k}_2 + \mathbf{k}_3 = \mathbf{0}$ at each z are reduced to 5 by the fixed observer's line of sight direction \mathbf{n} . The bispectrum can be chosen at each z to be a function of the 3 magnitudes $k_a = (k_1, k_2, k_3)$ and 2 angles that define the orientation of the triangle (see Fig. 1):

$$B_g(z, \mathbf{k}_a) = B_g(z, k_a, \mu_1, \varphi). \quad (1.3)$$

Here $\mu_a = \hat{\mathbf{k}}_a \cdot \mathbf{n} = \cos \theta_a$, and φ is the angle between the triangle plane and the $(\mathbf{n}, \mathbf{k}_1)$ -plane. The three angles $\theta_{ab} = \cos^{-1}(\hat{\mathbf{k}}_a \cdot \hat{\mathbf{k}}_b)$, are determined by k_a ; then $\mu_2 = \mu_1 \cos \theta_{12} + \sin \theta_1 \sin \theta_{12} \cos \varphi$ is determined when φ is given, and $\mu_3 = -(\mu_1 k_1 + \mu_2 k_2)/k_3$.

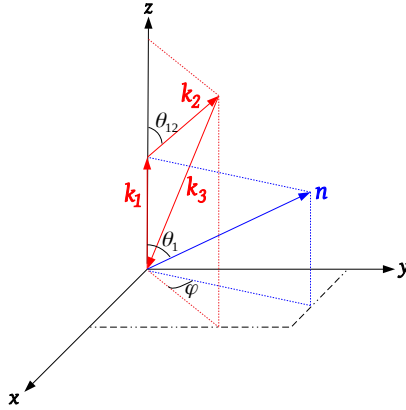


Figure 1. Relevant vectors and angles for the Fourier bispectrum.

In the standard Newtonian approximation, $B_g = B_{gN}$, the kernels in (1.2) contain the galaxy bias and the redshift-space distortions (RSD) at first and second order [3, 12]:

$$\mathcal{K}_N^{(1)}(\mathbf{k}_1) = b_1 + f \mu_1^2, \quad (1.4)$$

$$\mathcal{K}_N^{(2)}(\mathbf{k}_1, \mathbf{k}_2, \mathbf{k}_3) = b_1 F_2(\mathbf{k}_1, \mathbf{k}_2) + b_2 + f \mu_3^2 G_2(\mathbf{k}_1, \mathbf{k}_2) + f Z_2(\mathbf{k}_1, \mathbf{k}_2) + b_{s2} S_2(\mathbf{k}_1, \mathbf{k}_2), \quad (1.5)$$

where we dropped the z -dependence for brevity. Here f is the linear matter growth rate, b_1, b_2 are the linear and second-order clustering biases, and b_{s2} is the tidal bias. The kernel

F_2 is for second-order density, G_2, Z_2 are for RSD, and S_2 is the kernel for tidal bias (see the Appendix).

The Doppler-type relativistic corrections to the Newtonian number count contrast in redshift space are given at first order by [13]:

$$\delta_{gD} = A \mathbf{v} \cdot \mathbf{n}, \quad (1.6)$$

where $A(z)$ is given below in (1.12) and the momentum conservation equation has been used to eliminate the gravitational redshift: $\mathbf{n} \cdot \nabla \Phi \equiv \partial_r \Phi = -\mathbf{v}' \cdot \mathbf{n} - \mathcal{H} \mathbf{v} \cdot \mathbf{n}$. Here Φ is the gravitational potential, \mathbf{v} is the peculiar velocity, \mathcal{H} is the comoving Hubble parameter, and r is the line-of-sight comoving distance. Note that $\mathbf{v} \cdot \mathbf{n} = \partial_r V$, where V is the velocity potential ($v_i = \partial_i V$). At second order, and neglecting vector and tensor modes, it is shown in [8] that (see also [14])

$$\begin{aligned} \delta_{gD}^{(2)} = & A \mathbf{v}^{(2)} \cdot \mathbf{n} + 2C(\mathbf{v} \cdot \mathbf{n}) \delta + 2\frac{E}{\mathcal{H}}(\mathbf{v} \cdot \mathbf{n}) \partial_r(\mathbf{v} \cdot \mathbf{n}) + \frac{2}{\mathcal{H}^2}[(\mathbf{v} \cdot \mathbf{n}) \partial_r^2 \Phi - \Phi \partial_r^2(\mathbf{v} \cdot \mathbf{n})] \\ & - \frac{2}{\mathcal{H}} \partial_r(\mathbf{v} \cdot \mathbf{v}) + 2\frac{b_1}{\mathcal{H}} \Phi \partial_r \delta. \end{aligned} \quad (1.7)$$

The redshift-dependent coefficients C, E are given below in (1.13), (1.14).

In Fourier space, neglecting sub-leading $\mathcal{O}(\mathcal{H}^2/k^2)$ terms, we find from (1.2) that

$$\begin{aligned} B_{gD}(\mathbf{k}_1, \mathbf{k}_2, \mathbf{k}_3) = & \left\{ \left[\mathcal{K}_N^{(1)}(\mathbf{k}_1) \mathcal{K}_D^{(1)}(\mathbf{k}_2) + \mathcal{K}_D^{(1)}(\mathbf{k}_1) \mathcal{K}_N^{(1)}(\mathbf{k}_2) \right] \mathcal{K}_N^{(2)}(\mathbf{k}_1, \mathbf{k}_2, \mathbf{k}_3) \right. \\ & \left. + \mathcal{K}_N^{(1)}(\mathbf{k}_1) \mathcal{K}_N^{(1)}(\mathbf{k}_2) \mathcal{K}_D^{(2)}(\mathbf{k}_1, \mathbf{k}_2, \mathbf{k}_3) \right\} P(k_1) P(k_2) + 2 \text{ cp}. \end{aligned} \quad (1.8)$$

The relativistic kernels follow from (1.6) and (1.7); they are given in [8] as

$$\mathcal{K}_D^{(1)}(\mathbf{k}_1) = i \mathcal{H} f A \frac{\mu_1}{k_1}, \quad (1.9)$$

$$\begin{aligned} \mathcal{K}_D^{(2)}(\mathbf{k}_1, \mathbf{k}_2, \mathbf{k}_3) = & i \mathcal{H} f \left[A \frac{\mu_3}{k_3} G_2(\mathbf{k}_1, \mathbf{k}_2) + C \left(\frac{\mu_1}{k_1} + \frac{\mu_2}{k_2} \right) + \left(\frac{3}{2} \Omega_m - f E \right) \mu_1 \mu_2 \left(\frac{\mu_1}{k_2} + \frac{\mu_2}{k_1} \right) \right. \\ & \left. - \frac{3}{2} \Omega_m \left(\mu_1^3 \frac{k_1}{k_2^2} + \mu_2^3 \frac{k_2}{k_1^2} \right) + 2f \hat{\mathbf{k}}_1 \cdot \hat{\mathbf{k}}_2 \left(\frac{\mu_1}{k_1} + \frac{\mu_2}{k_2} \right) - \frac{3\Omega_m b_1}{2f} \left(\mu_1 \frac{k_1}{k_2^2} + \mu_2 \frac{k_2}{k_1^2} \right) \right] \end{aligned} \quad (1.10)$$

It is clear from (1.8)–(1.10) and from the general expressions given in [15, 16], that Doppler-type relativistic effects generate an imaginary correction to the Newtonian bispectrum:

$$\text{Re } B_g = B_{gN} + \mathcal{O}(\mathcal{H}^2/k^2), \quad i \text{Im } B_g = B_{gD} + \mathcal{O}(\mathcal{H}^3/k^3). \quad (1.11)$$

The coefficients in (1.9) and (1.10) are [8]

$$A = b_e - 2\mathcal{Q} + \frac{2(\mathcal{Q} - 1)}{r\mathcal{H}} - \frac{\mathcal{H}'}{\mathcal{H}^2}, \quad (1.12)$$

$$C = b_1(A + f) + \frac{b_1'}{\mathcal{H}} + 2 \left(1 - \frac{1}{r\mathcal{H}} \right) \frac{\partial b_1}{\partial \ln L} \Big|_c, \quad (1.13)$$

$$E = 4 - 2A - \frac{3}{2} \Omega_m, \quad (1.14)$$

where a prime is a conformal time derivative, $\Omega_m = \Omega_{m0}(1+z)H_0^2/\mathcal{H}^2$, L is the luminosity, and $|_c$ denotes evaluation at the flux cut.

In addition to the clustering bias b_1 , the relativistic bispectrum is sensitive to the evolution bias and magnification bias, which are defined as [17]

$$b_e = -\frac{\partial \ln n_g}{\partial \ln(1+z)}, \quad \mathcal{Q} = -\frac{\partial \ln n_g}{\partial \ln L} \Big|_c. \quad (1.15)$$

Here and below, n_g is the *comoving* galaxy number density. (Note that the alternative magnification bias parameter $s = 2\mathcal{Q}/5$ is often used.)

It is interesting to note that the magnification bias \mathcal{Q} enters the relativistic bispectrum, even though we have not included the effect of the integrated lensing magnification κ . The reason for this apparent inconsistency is that there is a (non-integrated) Doppler correction to κ at leading order [18, 19].

2 SIGNAL TO NOISE

The signal-to-noise ratio (SNR) for the bispectrum at redshift z is given in the Gaussian approximation of uncorrelated triangles by [20]

$$\left[\frac{S}{N}(z) \right]^2 = \sum_{k_a, \mu_1, \varphi} \frac{1}{\text{Var}[B_g(z, k_a, \mu_1, \varphi)]} B_g(z, k_a, \mu_1, \varphi) B_g^*(z, k_a, \mu_1, \varphi), \quad (2.1)$$

where we have introduced the complex conjugate B_g^* since the bispectrum has an imaginary correction. Here $\text{Var}[B_g]$ is the variance of the bispectrum estimator [21]:

$$\hat{B}_g(z, \mathbf{k}_a) = \frac{k_f^3}{V_{123}} \int_{\mathbf{k}_a} d^3 \mathbf{q}_1 d^3 \mathbf{q}_2 d^3 \mathbf{q}_3 \delta^{\text{Dirac}}(\mathbf{q}_1 + \mathbf{q}_2 + \mathbf{q}_3) \delta_g(z, \mathbf{q}_1) \delta_g(z, \mathbf{q}_2) \delta_g(z, \mathbf{q}_3), \quad (2.2)$$

where integration is over the shells $k_a - \Delta k/2 \leq q_a \leq k_a + \Delta k/2$ and the shell volume is $V_{123} = \int_{\mathbf{k}_a} d^3 \mathbf{q}_1 d^3 \mathbf{q}_2 d^3 \mathbf{q}_3 \delta^{\text{Dirac}}(\mathbf{q}_1 + \mathbf{q}_2 + \mathbf{q}_3)$.

In the Newtonian approximation, the Gaussian variance can be given as [3, 20]

$$\text{Var}[B_g(z, k_a, \mu_1, \varphi)] = s_B \frac{\pi k_f(z)^3}{k_1 k_2 k_3 (\Delta k)^3} \frac{N_{\mu_1} N_{\varphi}}{\Delta \mu_1 \Delta \varphi} \tilde{P}_{gN}(z, k_1, \mu_1) \tilde{P}_{gN}(z, k_2, \mu_2) \tilde{P}_{gN}(z, k_3, \mu_3), \quad (2.3)$$

where

$$\tilde{P}_{gN}(z, k_a, \mu_a) = P_{gN}(z, k_a, \mu_a) + \frac{1}{n_g(z)}, \quad (2.4)$$

and $P_{gN} = (b_1 + f\mu_a^2)^2 P$ is the linear galaxy power spectrum. In (2.3), s_B is 6, 2, 1 respectively for equilateral, isosceles and non-isosceles triangles, and N_{μ_1}, N_{φ} are the ranges for μ_1, φ (which are sometimes reduced from their full values of 2 and 2π using symmetry arguments). The fundamental mode is determined by the comoving survey volume of the redshift bin centred at z , i.e., $k_f(z) = 2\pi V(z)^{-1/3}$, where $V(z) = 4\pi f_{\text{sky}}[r(z + \Delta z/2)^3 - r(z - \Delta z/2)^3]$.

For a survey with redshift bin centres ranging from z_{\min} to z_{\max} , the cumulative SNR is

$$\frac{S}{N}(\leq z) = \left\{ \sum_{z'=z_{\min}}^z \left[\frac{S}{N}(z') \right]^2 \right\}^{1/2}, \quad (2.5)$$

and then the total SNR is $S/N(\leq z_{\max})$.

2.1 Relativistic contribution to the variance

For the full bispectrum, including the relativistic part, (2.2) leads to a variance of the form

$$\text{Var}[B_g(z, \mathbf{k}_a)] \propto \tilde{P}_g(z, k_1, \mu_1) \tilde{P}_g(z, k_2, \mu_2) \tilde{P}_g(z, k_3, \mu_3). \quad (2.6)$$

In the Newtonian approximation, this gives (2.3). By (1.9), the galaxy number density contrast has an imaginary relativistic correction, $\delta_g = \delta_{gN} + \delta_{gD}$. However, since $P_g \sim \langle \delta_g(\mathbf{k}) \delta_g(-\mathbf{k}) \rangle = \langle |\delta_g(\mathbf{k})|^2 \rangle$, the galaxy power spectrum is given by [7, 8, 11]

$$P_g = P_{gN} + P_{gD} = P_{gN} + \mathcal{O}(\mathcal{H}^2/k^2). \quad (2.7)$$

It follows from (2.6) and (2.7) that at leading order, the relativistic contribution to the variance can be neglected:

$$\text{Var}[B_g] = \text{Var}[B_{gN}] + \mathcal{O}(\mathcal{H}^2/k^2). \quad (2.8)$$

Therefore the SNR for the Newtonian and relativistic parts of the bispectrum are

$$\left(\frac{S}{N}\right)_N^2 = \sum_{k_a, \mu_1, \varphi} \frac{B_{gN} B_{gN}}{\text{Var}[B_{gN}]}, \quad (2.9)$$

$$\left(\frac{S}{N}\right)_D^2 = \sum_{k_a, \mu_1, \varphi} \frac{B_{gD} B_{gD}^*}{\text{Var}[B_{gN}]} \quad (2.10)$$

2.2 Nonlinear effects

In order to avoid nonlinear effects of matter clustering, the maximum k is chosen as a scale where perturbation theory for the matter density contrast begins to break down. It is known that the matter bispectrum is more sensitive to nonlinearity than the matter power spectrum: at $z \sim 0$ nonlinearity sets in at $k \sim 0.1h/\text{Mpc}$ for the matter bispectrum, as opposed to $k \sim 0.2h/\text{Mpc}$ for the matter power spectrum. To account for the growth of k_{max} with redshift, we use the redshift-dependence proposed in [22] for the power spectrum, but with half the amplitude at $z = 0$:

$$k_{\text{max}}(z) = 0.1h(1+z)^{2/(2+n_s)}. \quad (2.11)$$

The cut-off $k \leq k_{\text{max}}(z)$ avoids a breakdown of perturbative accuracy in the matter correlations, but nonlinearities in the galaxy correlations due to RSD can affect longer wavelength modes. The effect of RSD on these scales is to damp the power – the ‘FoG’ effect. In order to take account of this, we follow [3, 4] and use the simple model of FoG damping,

$$P_g \rightarrow D_P P_g, \quad D_P(z, \mathbf{k}) = \exp \left\{ -\frac{1}{2} [k\mu\sigma(z)]^2 \right\}, \quad (2.12)$$

$$B_g \rightarrow D_B B_g, \quad D_B(z, \mathbf{k}_1, \mathbf{k}_2, \mathbf{k}_3) = \exp \left\{ -\frac{1}{2} [k_1^2 \mu_1^2 + k_2^2 \mu_2^2 + k_3^2 \mu_3^2] \sigma(z)^2 \right\}, \quad (2.13)$$

where σ is the linear velocity dispersion.

On sufficiently large scales the non-Gaussian contribution to the bispectrum covariance can be approximated by including corrections to the power spectra appearing in the bispectrum variance (2.3). This is shown by [21] (see also [3]), using the approximation:

$$\text{Var}[B_g] \rightarrow \text{Var}[B_g] + \delta\text{Var}[B_g], \quad (2.14)$$

$$\delta\text{Var}[B_g] = \frac{s_B \pi k_f^3 N_{\mu_1} N_\varphi}{k_1 k_2 k_3 (\Delta k)^3 \Delta \mu_1 \Delta \varphi} \left\{ \tilde{P}_{gN}(1) \tilde{P}_{gN}(2) \left[\tilde{P}_{gN}^{\text{NL}}(3) - \tilde{P}_{gN}(3) \right] + 2 \text{cp} \right\}. \quad (2.15)$$

Here $\tilde{P}_{gN}(a) \equiv \tilde{P}_{gN}(z, k_a, \mu_a)$ and $\tilde{P}_{gN}^{\text{NL}}(a) = (b + f \mu_a^2)^2 P^{\text{NL}} + n_g^{-1}$, where P^{NL} is the nonlinear matter power spectrum, computed with a modified Halofit emulator.

2.3 Summations over triangles

The counting of triangles $\mathbf{k}_1 + \mathbf{k}_2 + \mathbf{k}_3 = \mathbf{0}$ that contribute to the signal-to-noise involves a sum in k_a -space and a sum over orientations.

The triangle sides are chosen so that $k_1 \geq k_2 \geq k_3$, and must satisfy $k_1 - k_2 - k_3 \leq 0$. For the summation in k_a we choose the minimum and the step-length as

$$k_{\min}(z) = k_f(z) \quad \text{and} \quad \Delta k(z) = k_f(z), \quad (2.16)$$

as in [3, 4]. Then the k_a sum is defined as [5, 23]

$$\sum_{k_a} = \sum_{k_1=k_{\min}}^{k_{\max}} \sum_{k_2=k_{\min}}^{k_1} \sum_{k_3=k_{\min}}^{k_2}. \quad (2.17)$$

The coordinates $(\mu_1 = \cos \theta_1, \varphi)$ describe all possible orientations of the triangle. We follow [3] and choose the ranges $N_{\mu_1} = 2, N_\varphi = 2\pi$. For a given μ_1 , a complete rotation in φ about \mathbf{k}_1 double counts the triangle falling onto the fixed $(\mathbf{n}, \mathbf{k}_1)$ -plane at $\varphi = 0$ and $\varphi = 2\pi$ (see Fig. 1). Similarly, for a given φ , the end-points $\theta_1 = 0$ and $\theta_1 = \pi$ correspond to equivalent triangles, with $\mathbf{k}_a \rightarrow -\mathbf{k}_a$. This double-counting can be avoided by imposing suitable upper limits: $-1 \leq \mu_1 < 1$ and $0 \leq \varphi < 2\pi$. The signal to noise is quite sensitive to the step-lengths $\Delta \mu_1, \Delta \varphi$. We find (see the Appendix for details) that a suitable choice for convergence is

$$\Delta \mu_1 = 0.04, \quad \Delta \varphi = \pi/25. \quad (2.18)$$

3 GALAXY SURVEY

We consider a Stage IV $H\alpha$ spectroscopic survey, with clustering bias, comoving volume, comoving number density and RSD damping parameter given by Table 1 in [4], over the redshift range $0.65 \leq z \leq 2.05$, with $\Delta z = 0.1$ bins. We provide fitting formulas for these quantities in the Appendix. Figure 2 shows the values given in [4] together with the fitting curves. For the cosmological parameters, we use Planck 2018 [24]: $h = 0.6766, \Omega_{m0} = 0.3111, \Omega_{b0} h^2 = 0.02242, \Omega_{c0} h^2 = 0.11933, n_s = 0.9665, \sigma_8 = 0.8102, \gamma = 0.545, \Omega_{K0} = 0 = \Omega_{\nu 0}$.

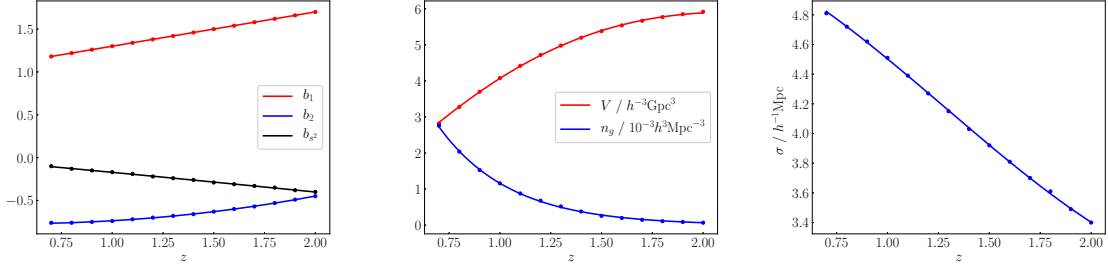


Figure 2. Clustering bias parameters (*left*), comoving volume and number density (*middle*) and RSD damping parameter (*right*). Points are the data from Table 1 in [4].

We checked that the SNR for the Newtonian bispectrum is consistent with Fig. 4 of [4], when we use their redshift-independent $k_{\text{max}} = 0.15h \text{ Mpc}^{-1}$, and when we remove the flattened triangle shapes that are excluded by [4]. When we include the flattened shapes, we checked that we recover the total number of triangles given in Table 1 of [5].

3.1 Evolution bias and magnification bias

The relativistic bispectrum depends also on b_e and \mathcal{Q} , as shown in (1.10)–(1.14). These parameters do *not* appear in the Newtonian approximation, but they are crucial for the relativistic correction, and we need to evaluate them in a physically consistent way. We compute these parameters from the same luminosity function that is used to generate the number density shown in Fig. 2, i.e., Model 1 in [25]:

$$\Phi(z, y) = \Phi_*(z) y^\alpha e^{-y}, \quad y \equiv \frac{L}{L_*}. \quad (3.1)$$

We have written Φ in terms of the redshift z and the normalised dimensionless luminosity y , where $L_* = L_{*0}(1+z)^\delta$ and L_{*0} is a characteristic luminosity. Here α is the faint-end slope, and Φ_* is a characteristic comoving density of $H\alpha$ emitters, modelled as

$$\frac{\Phi_*}{\Phi_{*0}} = \begin{cases} (1+z)^\epsilon & z \leq z_b, \\ (1+z_b)^{2\epsilon} (1+z)^{-\epsilon} & z > z_b. \end{cases} \quad (3.2)$$

The best-fit parameters for Model 1 are given by [25] as

$$\alpha = -1.35, \quad \delta = 2, \quad L_{*0} = 10^{41.5} \text{ erg s}^{-1}, \quad \Phi_{*0} = 10^{-2.8} \text{ Mpc}^{-3}, \quad \epsilon = 1, \quad z_b = 1.3. \quad (3.3)$$

The flux cut F_c translates to a luminosity cut:

$$L_c(z) = 4\pi F_c d_L(z)^2, \quad F_c = 3 \times 10^{-16} \text{ erg cm}^{-2} \text{ s}^{-1}, \quad (3.4)$$

where d_L is the background luminosity distance and the choice of F_c follows [4].

In order to compute b_e and \mathcal{Q} , we require the comoving number density

$$n_g(z) = \int_{y_c(z)}^{\infty} dy \Phi(z, y) = \Phi_*(z) \Gamma(\alpha + 1, y_c(z)), \quad (3.5)$$

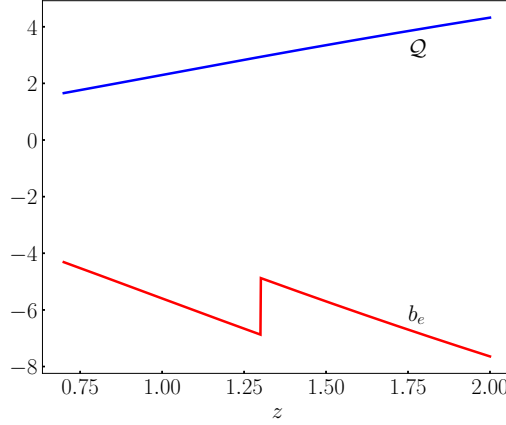


Figure 3. Magnification and evolution bias (3.7), (3.8).

where Γ is the upper incomplete Gamma function and

$$y_c(z) = \frac{4\pi F_c}{L_{*0}} r(z)^2 = \left[\frac{r(z)}{2.97 h \times 10^3 \text{ (Mpc/h)}} \right]^2. \quad (3.6)$$

Using (3.6) and (3.1)–(3.4), we confirm that the analytical form (3.5) for n_g recovers the points from Table 1 in [4].

By (1.15), the magnification bias follows as

$$\mathcal{Q}(z) = \left(y \frac{\Phi}{n_g} \right)_c = \frac{y_c(z)^{\alpha+1} \exp[-y_c(z)]}{\Gamma(\alpha+1, y_c(z))}, \quad (3.7)$$

since $\partial/\partial \ln L = \partial/\partial \ln y$, and the evolution bias is ¹ [26]

$$b_e(z) = -\frac{d \ln \Phi_*(z)}{d \ln(1+z)} - \frac{d \ln L_*(z)}{d \ln(1+z)} \mathcal{Q}(z). \quad (3.8)$$

Figure 3 shows the analytical forms (3.7) and (3.8) for b_e and \mathcal{Q} .

Table 1 collects the information in Figs. 2 and 3 to provide an extension of Table 1 in [4].

Finally, we need to deal with the luminosity derivative of the bias in (1.13). Simulations by [27] indicate that the clustering bias of $H\alpha$ galaxies does not vary appreciably with luminosity near the fiducial luminosity L_{*0} in (3.3) and for $z \lesssim 2$ (see their Fig. 8). We therefore take

$$\left. \frac{\partial b_1}{\partial \ln L} \right|_c = 0, \quad (3.9)$$

in (1.13).

¹Error in equation (3.8) fixed - results unchanged.

Table 1. Stage IV $H\alpha$ spectroscopic survey parameters.

z	b_1	b_2	b_{s^2}	b_e	\mathcal{Q}	n_g $10^{-3}h^3\text{Mpc}^{-3}$	V $h^{-3}\text{Gpc}^3$	σ $h^{-1}\text{Mpc}$
0.7	1.18	-0.766	-0.105	-4.31	1.66	2.76	2.82	4.81
0.8	1.22	-0.759	-0.127	-4.74	1.87	2.04	3.38	4.72
0.9	1.26	-0.749	-0.149	-5.17	2.08	1.53	3.70	4.62
1.0	1.30	-0.737	-0.172	-5.60	2.30	1.16	4.08	4.51
1.1	1.34	-0.721	-0.194	-6.02	2.51	0.880	4.42	4.39
1.2	1.38	-0.703	-0.217	-6.45	2.72	0.680	4.72	4.27
1.3	1.42	-0.682	-0.240	-6.76	2.94	0.520	4.98	4.15
1.4	1.46	-0.658	-0.262	-5.29	3.14	0.380	5.20	4.03
1.5	1.50	-0.631	-0.285	-5.70	3.35	0.260	5.38	3.92
1.6	1.54	-0.600	-0.308	-6.10	3.55	0.200	5.54	3.81
1.7	1.58	-0.567	-0.332	-6.50	3.75	0.150	5.67	3.70
1.8	1.62	-0.531	-0.355	-6.89	3.94	0.110	5.77	3.61
1.9	1.66	-0.491	-0.378	-7.27	4.13	0.0900	5.85	3.49
2.0	1.70	-0.449	-0.401	-7.64	4.32	0.0700	6.92	3.40

3.2 Signal to noise of the relativistic bispectrum

We can now evaluate the Doppler-type relativistic part of the bispectrum, (1.8)–(1.14), using (3.7)–(3.9). Then the SNR is computed using (2.5) and (2.10) together with (2.15). The results, for SNR in each z -bin, $S/N(z)$, and for the cumulative SNR, $S/N(\leq z)$, are shown in Fig. 4. Our forecasts indicate that the total SNR, $S/N(\leq z_{\text{max}})$, for a Stage IV $H\alpha$ survey could be $\mathcal{O}(10)$, which is high enough for a detection in principle.

The relativistic SNR is sensitive in particular to two factors:

- Changes in the nonperturbative scale $k_{\text{max}}(z)$: this sensitivity is due to the coupling of long-wavelength relativistic terms to short-wavelength Newtonian terms. We use a conservative and redshift-dependent k_{max} , given in (2.11). In Fig. 5 we show the comparison of SNR using (2.11) and using the redshift-independent $k_{\text{max}} = 0.15h/\text{Mpc}$. The redshift-independent model does not incorporate the increase in the nonperturbative scale with growing z , and therefore produces a lower SNR; however, the difference is not large.
- Changes in $b_e(z)$, $\mathcal{Q}(z)$: In the Appendix (Fig. 10) we illustrate the significant impact on cumulative SNR of changing b_e , \mathcal{Q} . We use a range of constant choices for b_e , \mathcal{Q} – which are not physically motivated. This shows the importance of modelling b_e , \mathcal{Q} self-consistently from the same luminosity function that produces the number density, as we have done.

The sensitivity of the relativistic SNR to k_{max} reflects the importance of the coupling of the relativistic signal to Newtonian terms on short scales. How sensitive is the SNR to the signal on the largest scales? We can answer this by increasing k_{min} from its fiducial value k_{f} , which is the maximal observable scale. The result is that there is only a small reduction when $k_{\text{min}}/k_{\text{f}}$ is increased by a factor up to 5, as shown in Fig. 6. Even with $k_{\text{min}} = 10k_{\text{f}}$,

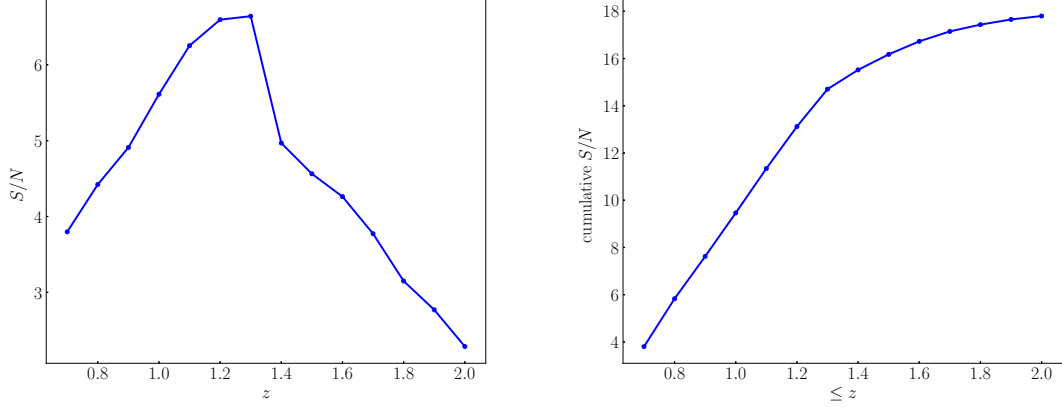


Figure 4. Relativistic SNR per z -bin (*left*) and cumulative (*right*) for a Stage IV $H\alpha$ survey.

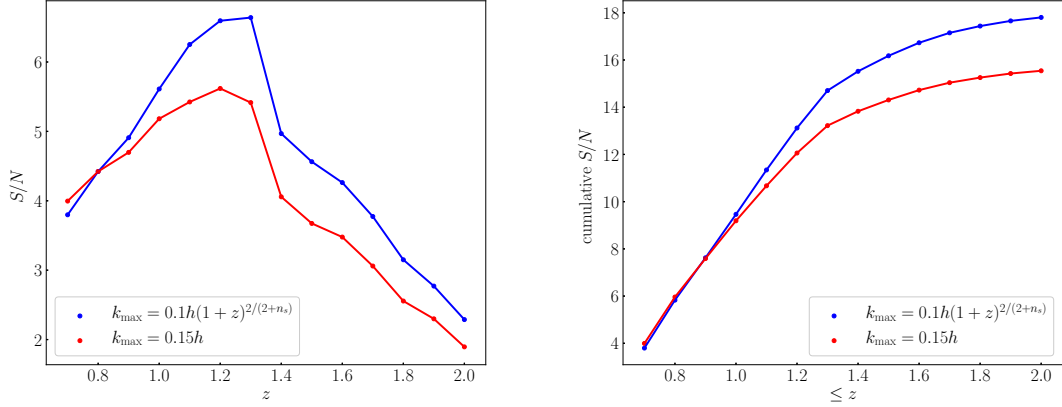


Figure 5. Effect of changing k_{\max} on SNR per bin (*left*) and cumulative SNR (*right*).

the total SNR is ~ 10 . This means that the relativistic SNR does not depend critically on accessing the largest possible scales.

It is also interesting to investigate how important for the SNR is the second-order relativistic contribution in the bispectrum, i.e. from terms of the form

$$\mathcal{K}_N^{(1)}(\mathbf{k}_1)\mathcal{K}_N^{(1)}(\mathbf{k}_2)\mathcal{K}_D^{(2)}(\mathbf{k}_1, \mathbf{k}_2, \mathbf{k}_3), \quad (3.10)$$

in (1.8), compared to the first-order contribution, i.e. from terms of the form

$$\left[\mathcal{K}_N^{(1)}(\mathbf{k}_1)\mathcal{K}_D^{(1)}(\mathbf{k}_2) + \mathcal{K}_D^{(1)}(\mathbf{k}_1)\mathcal{K}_N^{(1)}(\mathbf{k}_2) \right] \mathcal{K}_N^{(2)}(\mathbf{k}_1, \mathbf{k}_2, \mathbf{k}_3). \quad (3.11)$$

It is conceivable that the first-order Doppler-type contribution in (3.11) to B_g , which couples to first- and second-order Newtonian terms, dominates the SNR. However, we find that the first- and second-order relativistic parts of the bispectrum make comparable contributions to the SNR – see Fig. 7. We deduce that the second-order relativistic contribution in (3.10)

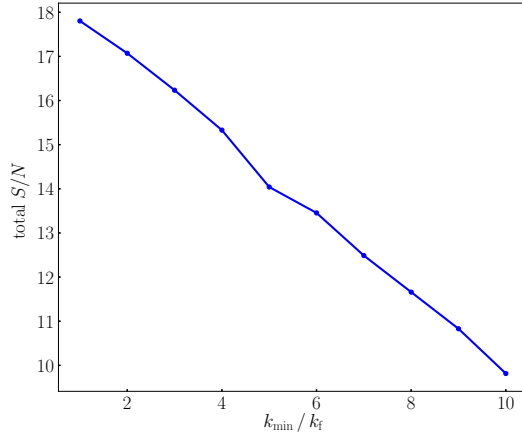


Figure 6. Effect of changing k_{\min} on total relativistic SNR.

cannot be neglected. Furthermore, this means that it must be accurately modelled, as we have done.

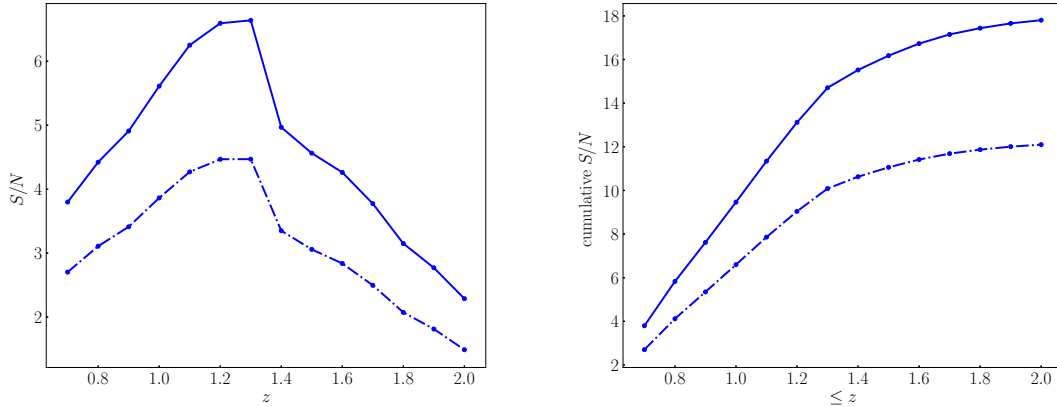


Figure 7. As in Fig. 4, but showing the effect of omitting the second-order relativistic contribution (3.10) to the bispectrum (dot-dashed curves).

Recently [9] estimated the SNR for the leading relativistic part of the bispectrum. There are significant differences in their analysis compared to ours. In particular, they neglect most of the terms in $\delta_{gD}^{(2)}$ [see our (1.7)] which defines $\mathcal{K}_D^{(2)}$ (see the Appendix for further details). In addition they do not use self-consistent models for b_e and \mathcal{Q} . These two differences could account for their conclusion that the relativistic signal is not detectable, in contrast to our result.

An interesting feature of the relativistic signal is that there is a significant contribution to the SNR from flattened triangle shapes. This is consistent with the results of [8] for the dipole that is generated by the imaginary part of the bispectrum.

3.3 Including cosmological parameters

A full treatment of cosmological constraints would marginalise over the standard cosmo-

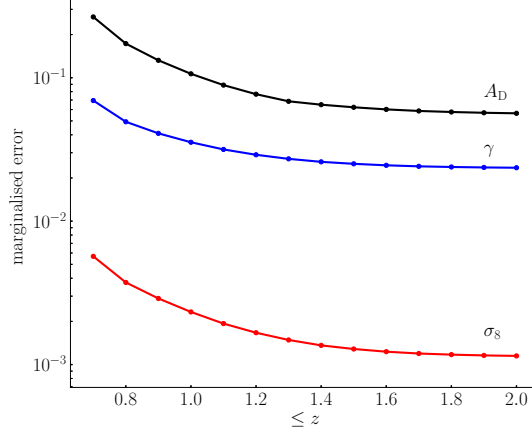


Figure 8. Marginal errors (cumulative) on the relativistic contribution, growth index and clustering amplitude, using the full bispectrum.

logical parameters, together with the Alcock-Paczynski parameters and the clustering bias parameters. The constraints obtained would depend almost entirely on the Newtonian galaxy power spectrum and bispectrum (as analysed in [4]), given that the relativistic contribution to the power spectrum is below leading order, while in the bispectrum the relativistic SNR is an order of magnitude smaller than the Newtonian SNR.

Our focus here is instead on the detectability of the relativistic signal in the bispectrum, assuming that P_{gN} and B_{gN} have been used to constrain the standard parameters. We now investigate the effect on this detectability when we include the parameters directly related to redshift-space effects, i.e., the growth index $\gamma = \ln f / \ln \Omega_m$ (with fiducial value 0.545), and the clustering amplitude σ_8 (with Planck 2018 fiducial). For forecasts we use the theoretical values of b_e, \mathcal{Q} . In a galaxy survey, they would be measured directly from the observed luminosity function, and their measurement uncertainties would need to be marginalised over.

For the relativistic part of the bispectrum, we introduce a parameter A_D , with fiducial value 1:

$$B_g = B_{gN} + A_D B_{gD}. \quad (3.12)$$

Then the Fisher matrix for the parameters $\vartheta_\alpha = (A_D, \gamma, \sigma_8)$ is

$$F_{\alpha\beta} = \sum_{z, k_a, \mu_1, \varphi} \frac{1}{\text{Var}[B_g]} \frac{\partial B_g}{\partial \vartheta_{(\alpha}} \frac{\partial B_g^*}{\partial \vartheta_{\beta)}, \quad (3.13)$$

where the round brackets denote symmetrisation. The cumulative marginal errors $\sigma_\alpha = [(F^{-1})_{\alpha\alpha}]^{1/2}$ are shown in Fig. 8. The fact that $\sigma_{A_D} \lesssim 0.1$ means that the relativistic effects remain detectable when the two additional cosmological parameters are marginalised over.

4 CONCLUSIONS

As shown by [8], the tree-level galaxy bispectrum in Fourier space has an imaginary part which is a unique signal of the leading-order relativistic corrections in redshift space. These corrections arise from Doppler and other line-of-sight effects on the past lightcone [see (1.6), (1.7)]. In the galaxy bispectrum, the corrections scale as $i(\mathcal{H}/k)P^2$, where P is the linear matter power spectrum [see (1.8)–(1.10)]. By contrast, at leading order in the galaxy power spectrum, the relativistic correction is real and scales as $(\mathcal{H}/k)^2P$ – i.e., it is suppressed by a further factor of \mathcal{H}/k . Only the cross-power spectrum of two different tracers produces an imaginary contribution that scales as $i(\mathcal{H}/k)P$ [7].²

For a single tracer, the $(\mathcal{H}/k)^2$ relativistic signal in the galaxy *power* spectrum is not detectable, even for a cosmic-variance limited survey [17]. The galaxy bispectrum of a single tracer, with its $i(\mathcal{H}/k)$ relativistic contribution, improves the chances of detectability. In addition, the relativistic contribution in the bispectrum couples to short-scale Newtonian terms – which means that the signal is not confined to very large scales, unlike the case of the power spectrum. We confirmed the expectations of detectability by showing that the signal to noise on the imaginary relativistic part is $\mathcal{O}(10)$ for a Stage IV $H\alpha$ spectroscopic survey similar to Euclid [see Fig. 4]. We checked that detectability is not compromised by including the uncertainties on two cosmological growth parameters, σ_8 and γ [Fig. 8], assuming that other cosmological and nuisance parameters are determined by the Newtonian power spectrum and bispectrum.

The relativistic SNR depends on the $k_{\max}(z)$ assumed, because of the coupling of relativistic effects to short-scale Newtonian terms [Fig. 5], and we made a conservative choice (2.11), which includes a redshift dependence to reflect the weakening of nonlinearity at higher z . Accurate modelling of nonlinear effects would allow us to increase the SNR – this is not at all specific to the relativistic signal, but is required for the standard analysis of RSD.

The relativistic SNR also relies on the largest available scales, but very little signal is lost if k_{\min}/k_f is increased by a factor up to 5, and even a factor of 10 increase leaves a detectable SNR [Fig. 6].

By contrast, the SNR depends strongly on accurate modelling of the second-order part of the relativistic correction [Fig. 7]. This includes both the theoretical form (1.7), and the two astrophysical parameters that do not appear in the Newtonian approximation of the galaxy bispectrum: the evolution bias b_e (measuring the deviation from comoving number conservation) and the magnification bias \mathcal{Q} (which is brought into play by a Doppler correction to standard lensing magnification). A key feature of our analysis is a physically self-consistent derivation of these quantities from the luminosity function [Fig. 3 and (3.7), (3.8)]. We showed that the SNR is very sensitive to these parameters [Fig. 10], which underlines the need for accurate physical modelling.

We assumed a Gaussian covariance in our computations, but we used the approximation of [21] to include non-Gaussian corrections.

Further work should include the window function which we have neglected. The imaginary part of the galaxy bispectrum generates a dipole, as shown in [8]. This suggests a multipole analysis that uses the relativistic dipole in addition to the monopole and quadrupole, which are unaffected by relativistic effects at leading order. The window function can also have an imaginary part [37], which will need to be corrected for. The dipole from the imag-

²See also [28–35] for the corresponding effect in the two-point correlation function, and see [36] for an imaginary short-scale contribution from neutrino drag on haloes.

inary part of the bispectrum vanishes in equilateral configurations [8], which may help to disentangle the relativistic dipole from that of the window function.

Our analysis, in common with other works on the Fourier bispectrum, implicitly uses the plane-parallel approximation, since the line-of-sight direction \mathbf{n} is fixed. At the cost of significant complexity, the approximation can be avoided, for example by using a Fourier-Bessel analysis of bispectrum multipoles [38]. Further work is needed to address this, but we note that errors from the approximation are mitigated in high redshift surveys such as the one considered here.

Finally, further work also needs to include the effects of lensing magnification, which are excluded in the standard Fourier analysis, but have been included in the galaxy angular bispectrum [39–42] and in a spherical Bessel analysis [43].

Acknowledgements

We thank Dionysis Karagiannis and Shun Saito for very helpful comments. RM and SJ are supported by the South African Radio Astronomy Observatory (SARAO) and the National Research Foundation (Grant No. 75415). RM and OU are supported by the UK Science & Technology Facilities Council (STFC) Consolidated Grants ST/N000668/1 and ST/K0090X/1. CC is supported by STFC Consolidated Grant ST/P000592/1. SC acknowledges support from the ‘Departments of Excellence 2018-2022’ Grant (L. 232/2016) awarded by the Italian Ministry of Education, University and Research (MIUR). SC is funded by MIUR through the Rita Levi Montalcini project ‘PROMETHEUS – Probing and Relating Observables with Multi-wavelength Experiments To Help Enlightening the Universe’s Structure’.

A APPENDIX

Newtonian kernels in (1.5)

$$F_2(\mathbf{k}_1, \mathbf{k}_2) = \frac{10}{7} + \hat{\mathbf{k}}_1 \cdot \hat{\mathbf{k}}_2 \left(\frac{k_1}{k_2} + \frac{k_2}{k_1} \right) + \frac{4}{7} (\hat{\mathbf{k}}_1 \cdot \hat{\mathbf{k}}_2)^2, \quad (\text{A.1})$$

$$G_2(\mathbf{k}_1, \mathbf{k}_2) = \frac{6}{7} + \hat{\mathbf{k}}_1 \cdot \hat{\mathbf{k}}_2 \left(\frac{k_1}{k_2} + \frac{k_2}{k_1} \right) + \frac{8}{7} (\hat{\mathbf{k}}_1 \cdot \hat{\mathbf{k}}_2)^2, \quad (\text{A.2})$$

$$Z_2(\mathbf{k}_1, \mathbf{k}_2) = f \frac{\mu_1 \mu_2}{k_1 k_2} (\mu_1 k_1 + \mu_2 k_2)^2 + \frac{b_1}{k_1 k_2} [(\mu_1^2 + \mu_2^2) k_1 k_2 + \mu_1 \mu_2 (k_1^2 + k_2^2)], \quad (\text{A.3})$$

$$S_2(\mathbf{k}_1, \mathbf{k}_2) = (\hat{\mathbf{k}}_1 \cdot \hat{\mathbf{k}}_2)^2 - \frac{1}{3}. \quad (\text{A.4})$$

Fitting formulas for Fig. 2 curves

$$b_1(z) = 0.9 + 0.4z, \quad b_2(z) = -0.741 - 0.125z + 0.123z^2 + 0.00637z^3, \quad (\text{A.5})$$

$$b_{s2}(z) = 0.0409 - 0.199z - 0.0166z^2 + 0.00268z^3, \quad (\text{A.6})$$

$$V(z) = 8.85 z^{1.65} \exp(-0.777z) h^{-3} \text{Gpc}^3, \quad (\text{A.7})$$

$$n_g(z) = 0.0193 z^{-0.0282} \exp(-2.81z) h^3 \text{Mpc}^{-3}, \quad (\text{A.8})$$

$$\sigma(z) = (5.29 - 0.249z - 0.720z^2 + 0.187z^3) h^{-1} \text{Mpc}. \quad (\text{A.9})$$

Number of orientation bins

Figure 9 shows the effect on the relativistic total SNR of changing the number of orientation bins, $n_{\mu_1} = N_{\mu_1}/\Delta\mu_1 = 2/\Delta\mu_1$ and $n_\varphi = N_\varphi/\Delta\varphi = 2\pi/\Delta\varphi$. It is apparent that reducing the number of bins increases the cumulative SNR. The cumulative SNR converges towards a minimum for $n_{\mu_1}, n_\varphi > 40$. We choose $n_{\mu_1} = n_\varphi = 50$, which is equivalent to (2.18).

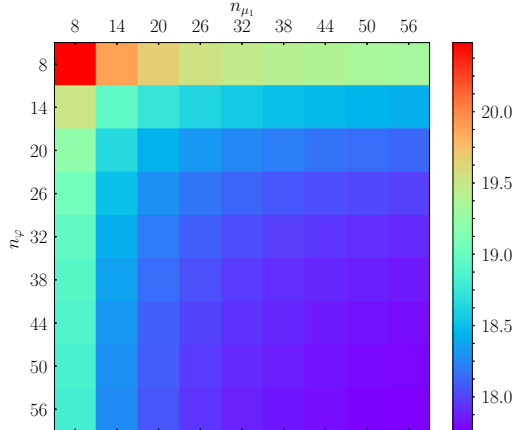


Figure 9. Effect on total relativistic SNR of changing number of φ and μ_1 bins.

Effect of changing magnification and evolution biases

The effect on the relativistic SNR of changes in magnification bias and in evolution bias is illustrated in Fig. 10.

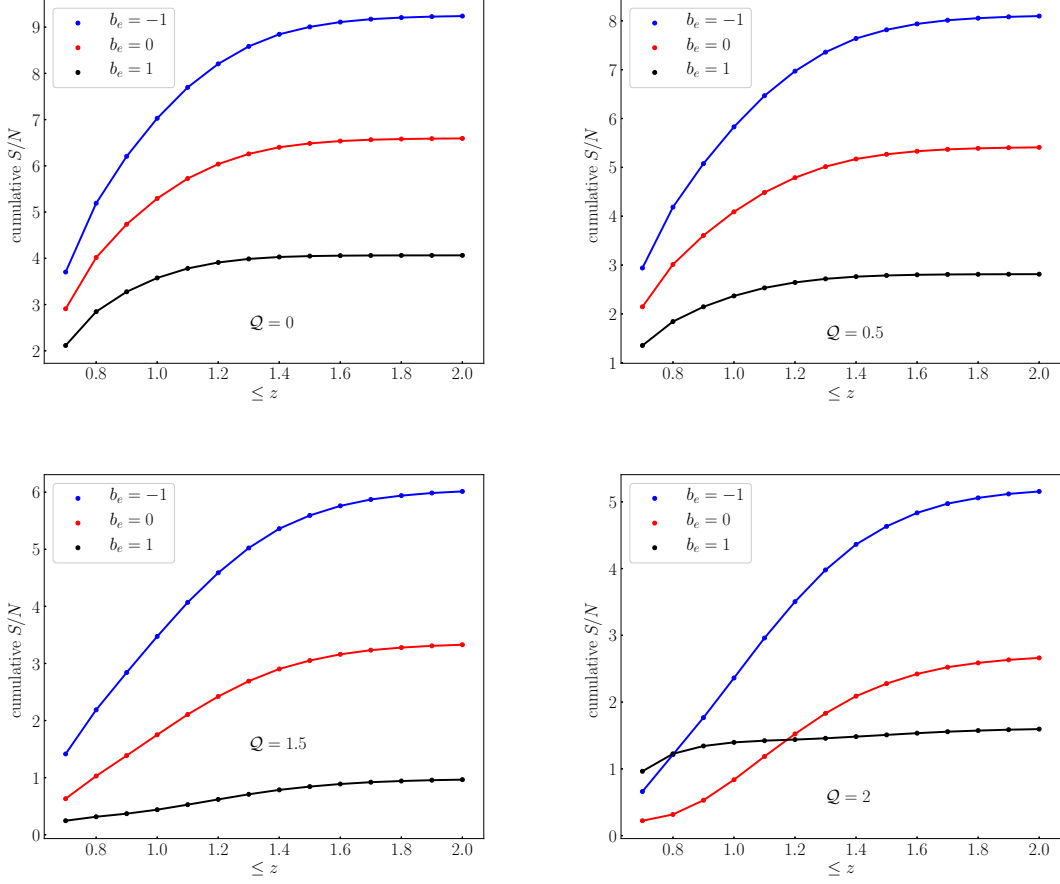


Figure 10. Effect of changing Q and b_e on relativistic cumulative SNR.

Comparison with [9]

In [9], a significant number of terms is neglected in the relativistic second-order galaxy number count contrast, $\delta_{gD}^{(2)}$, given by our (1.7). (Note that our (1.7), derived in [8], was independently confirmed by [14]). They have the first term, $A \mathbf{v}^{(2)} \cdot \mathbf{n}$, on the right of (1.7). In the second term, $2C(\mathbf{v} \cdot \mathbf{n}) \delta$, they do not have the correct form of the coefficient C – they include only the first part, $b_1 A$, of C [see the right-hand side of (1.13)]. All terms after the second term in (1.7) are omitted by [9]. Note that none of the omitted terms is suppressed by a higher power of k^{-1} ; they all have the same scaling, i.e., $\propto (\mathcal{H}/k) (\delta)^2$. In detail, they omit the following terms:

$$\begin{aligned}
 \delta_{gD}^{(2)}(\text{us}) - \delta_{gD}^{(2)}([9]) = & 2 \left[b_1 f + \frac{b'_1}{\mathcal{H}} + 2 \left(1 - \frac{1}{r\mathcal{H}} \right) \frac{\partial b_1}{\partial \ln L} \Big|_c \right] (\mathbf{v} \cdot \mathbf{n}) \delta \\
 & + \frac{2}{\mathcal{H}} \left(4 - 2A - \frac{3}{2} \Omega_m \right) (\mathbf{v} \cdot \mathbf{n}) \partial_r (\mathbf{v} \cdot \mathbf{n}) \\
 & + \frac{2}{\mathcal{H}^2} [(\mathbf{v} \cdot \mathbf{n}) \partial_r^2 \Phi - \Phi \partial_r^2 (\mathbf{v} \cdot \mathbf{n})] - \frac{2}{\mathcal{H}} \partial_r (\mathbf{v} \cdot \mathbf{v}) + 2 \frac{b_1}{\mathcal{H}} \Phi \partial_r \delta.
 \end{aligned} \tag{A.10}$$

References

- [1] H. Gil-Marín, W. J. Percival, L. Verde, J. R. Brownstein, C.-H. Chuang, F.-S. Kitaura, S. A. Rodríguez-Torres, and M. D. Olmstead, *The clustering of galaxies in the SDSS-III Baryon Oscillation Spectroscopic Survey: RSD measurement from the power spectrum and bispectrum of the DR12 BOSS galaxies*, *Mon. Not. Roy. Astron. Soc.* **465** (2017), no. 2 1757–1788, [[arXiv:1606.00439](#)].
- [2] N. S. Sugiyama, S. Saito, F. Beutler, and H.-J. Seo, *A complete FFT-based decomposition formalism for the redshift-space bispectrum*, *Mon. Not. Roy. Astron. Soc.* **484** (2019), no. 1 364–384, [[arXiv:1803.02132](#)].
- [3] D. Karagiannis, A. Lazanu, M. Liguori, A. Raccanelli, N. Bartolo, and L. Verde, *Constraining primordial non-Gaussianity with bispectrum and power spectrum from upcoming optical and radio surveys*, *Mon. Not. Roy. Astron. Soc.* **478** (2018), no. 1 1341–1376, [[arXiv:1801.09280](#)].
- [4] V. Yankelevich and C. Porciani, *Cosmological information in the redshift-space bispectrum*, *Mon. Not. Roy. Astron. Soc.* **483** (2019), no. 2 2078–2099, [[arXiv:1807.07076](#)].
- [5] A. Oddo, E. Sefusatti, C. Porciani, P. Monaco, and A. G. Sánchez, *Toward a robust inference method for the galaxy bispectrum: likelihood function and model selection*, *JCAP* **03** (2020) 056, [[arXiv:1908.01774](#)].
- [6] N. S. Sugiyama, S. Saito, F. Beutler, and H.-J. Seo, *Perturbation theory approach to predict the covariance matrices of the galaxy power spectrum and bispectrum in redshift space*, [[arXiv:1908.06234](#)].
- [7] P. McDonald, *Gravitational redshift and other redshift-space distortions of the imaginary part of the power spectrum*, *JCAP* **0911** (2009) 026, [[arXiv:0907.5220](#)].
- [8] C. Clarkson, E. M. de Weerd, S. Jolicoeur, R. Maartens, and O. Umeh, *The dipole of the galaxy bispectrum*, *Mon. Not. Roy. Astron. Soc.* **486** (2019), no. 1 L101–L104, [[arXiv:1812.09512](#)].
- [9] D. Jeong and F. Schmidt, *The Odd-Parity Galaxy Bispectrum*, [[arXiv:1906.05198](#)].
- [10] D. Jeong, F. Schmidt, and C. M. Hirata, *Large-scale clustering of galaxies in general relativity*, *Phys. Rev.* **D85** (2012) 023504, [[arXiv:1107.5427](#)].
- [11] L. R. Abramo and D. Bertacca, *Disentangling the effects of Doppler velocity and primordial non-Gaussianity in galaxy power spectra*, *Phys. Rev.* **D96** (2017), no. 12 123535, [[arXiv:1706.01834](#)].
- [12] F. Bernardeau, S. Colombi, E. Gaztanaga, and R. Scoccimarro, *Large scale structure of the universe and cosmological perturbation theory*, *Phys. Rept.* **367** (2002) 1–248, [[astro-ph/0112551](#)].
- [13] C. Bonvin and R. Durrer, *What galaxy surveys really measure*, *Phys. Rev.* **D84** (2011) 063505, [[arXiv:1105.5280](#)].
- [14] E. Di Dio and U. Seljak, *The relativistic dipole and gravitational redshift on LSS*, *JCAP* **1904** (2019), no. 04 050, [[arXiv:1811.03054](#)].
- [15] O. Umeh, S. Jolicoeur, R. Maartens, and C. Clarkson, *A general relativistic signature in the galaxy bispectrum: the local effects of observing on the lightcone*, *JCAP* **1703** (2017) 003, [[arXiv:1610.03351](#)].
- [16] S. Jolicoeur, O. Umeh, R. Maartens, and C. Clarkson, *Imprints of local lightcone projection effects on the galaxy bispectrum. II*, *JCAP* **1709** (2017) 040, [[arXiv:1703.09630](#)].
- [17] D. Alonso, P. Bull, P. G. Ferreira, R. Maartens, and M. Santos, *Ultra large-scale cosmology in next-generation experiments with single tracers*, *Astrophys. J.* **814** (2015), no. 2 145, [[arXiv:1505.07596](#)].

- [18] C. Bonvin, *Effect of Peculiar Motion in Weak Lensing*, *Phys. Rev.* **D78** (2008) 123530, [[arXiv:0810.0180](#)].
- [19] K. Bolejko, C. Clarkson, R. Maartens, D. Bacon, N. Meures, and E. Beynon, *Antilensing: The Bright Side of Voids*, *Phys. Rev. Lett.* **110** (2013), no. 2 021302, [[arXiv:1209.3142](#)].
- [20] R. Scoccimarro, E. Sefusatti, and M. Zaldarriaga, *Probing primordial non-Gaussianity with large-scale structure*, *Phys. Rev.* **D69** (2004) 103513, [[astro-ph/0312286](#)].
- [21] K. C. Chan and L. Blot, *Assessment of the Information Content of the Power Spectrum and Bispectrum*, *Phys. Rev.* **D96** (2017), no. 2 023528, [[arXiv:1610.06585](#)].
- [22] **VIRGO Consortium** Collaboration, R. E. Smith, J. A. Peacock, A. Jenkins, S. D. M. White, C. S. Frenk, F. R. Pearce, P. A. Thomas, G. Efstathiou, and H. M. P. Couchmann, *Stable clustering, the halo model and nonlinear cosmological power spectra*, *Mon. Not. Roy. Astron. Soc.* **341** (2003) 1311, [[astro-ph/0207664](#)].
- [23] M. Liguori, E. Sefusatti, J. R. Fergusson, and E. P. S. Shellard, *Primordial non-Gaussianity and Bispectrum Measurements in the Cosmic Microwave Background and Large-Scale Structure*, *Adv. Astron.* **2010** (2010) 980523, [[arXiv:1001.4707](#)].
- [24] **Planck** Collaboration, N. Aghanim et al., *Planck 2018 results. VI. Cosmological parameters*, [[arXiv:1807.06209](#)].
- [25] L. Pozzetti, C. M. Hirata, J. E. Geach, A. Cimatti, C. Baugh, O. Cucciati, A. Merson, P. Norberg, and D. Shi, *Modelling the number density of H α emitters for future spectroscopic near-IR space missions*, *Astron. Astrophys.* **590** (2016) A3, [[arXiv:1603.01453](#)].
- [26] R. Maartens, J. Fonseca, S. Camera, S. Jolicoeur, J.-A. Viljoen, and C. Clarkson, *Magnification and evolution biases in large-scale structure surveys*, [[arXiv:2107.13401](#)].
- [27] H. Pan, D. Obreschkow, C. Howlett, C. d. P. Lagos, P. J. Elahi, C. Baugh, and V. Gonzalez-Perez, *Multi-wavelength consensus of large-scale linear bias*, [[arXiv:1909.12069](#)].
- [28] C. Bonvin, L. Hui, and E. Gaztanaga, *Asymmetric galaxy correlation functions*, *Phys. Rev.* **D89** (2014), no. 8 083535, [[arXiv:1309.1321](#)].
- [29] C. Bonvin, L. Hui, and E. Gaztanaga, *Optimising the measurement of relativistic distortions in large-scale structure*, *JCAP* **1608** (2016), no. 08 021, [[arXiv:1512.03566](#)].
- [30] E. Gaztanaga, C. Bonvin, and L. Hui, *Measurement of the dipole in the cross-correlation function of galaxies*, *JCAP* **1701** (2017), no. 01 032, [[arXiv:1512.03918](#)].
- [31] V. Irsic, E. Di Dio, and M. Viel, *Relativistic effects in Lyman- α forest*, *JCAP* **1602** (2016), no. 02 051, [[arXiv:1510.03436](#)].
- [32] A. Hall and C. Bonvin, *Measuring cosmic velocities with 21 cm intensity mapping and galaxy redshift survey cross-correlation dipoles*, *Phys. Rev.* **D95** (2017), no. 4 043530, [[arXiv:1609.09252](#)].
- [33] F. Lepori, E. Di Dio, E. Villa, and M. Viel, *Optimal galaxy survey for detecting the dipole in the cross-correlation with 21 cm Intensity Mapping*, *JCAP* **1805** (2018), no. 05 043, [[arXiv:1709.03523](#)].
- [34] C. Bonvin and P. Fleury, *Testing the equivalence principle on cosmological scales*, *JCAP* **1805** (2018), no. 05 061, [[arXiv:1803.02771](#)].
- [35] F. Lepori, V. Irsic, E. Di Dio, and M. Viel, *The impact of relativistic effects on the 3D Quasar-Lyman- α cross-correlation*, [[arXiv:1910.06305](#)].
- [36] C. Okoli, M. I. Scrimgeour, N. Afshordi, and M. J. Hudson, *Dynamical friction in the primordial neutrino sea*, *Mon. Not. Roy. Astron. Soc.* **468** (2017), no. 2 2164–2175, [[arXiv:1611.04589](#)].

- [37] F. Beutler, E. Castorina, and P. Zhang, *Interpreting measurements of the anisotropic galaxy power spectrum*, *JCAP* **1903** (2019), no. 03 040, [[arXiv:1810.05051](#)].
- [38] E. Castorina and M. White, *Beyond the plane-parallel approximation for redshift surveys*, *Mon. Not. Roy. Astron. Soc.* **476** (2018), no. 4 4403–4417, [[arXiv:1709.09730](#)].
- [39] A. Kehagias, A. M. Dizgah, J. Norena, H. Perrier, and A. Riotto, *A Consistency Relation for the Observed Galaxy Bispectrum and the Local non-Gaussianity from Relativistic Corrections*, *JCAP* **1508** (2015), no. 08 018, [[arXiv:1503.04467](#)].
- [40] E. Di Dio, R. Durrer, G. Marozzi, and F. Montanari, *The bispectrum of relativistic galaxy number counts*, *JCAP* **1601** (2016) 016, [[arXiv:1510.04202](#)].
- [41] E. Di Dio, H. Perrier, R. Durrer, G. Marozzi, A. M. Dizgah, J. Norena, and A. Riotto, *Non-Gaussianities due to Relativistic Corrections to the Observed Galaxy Bispectrum*, *JCAP* **1703** (2017), no. 03 006, [[arXiv:1611.03720](#)].
- [42] E. Di Dio, R. Durrer, R. Maartens, F. Montanari, and O. Umeh, *The Full-Sky Angular Bispectrum in Redshift Space*, *JCAP* **2019** (2019), no. 04 053, [[arXiv:1812.09297](#)].
- [43] D. Bertacca, A. Raccanelli, N. Bartolo, M. Liguori, S. Matarrese, and L. Verde, *Relativistic wide-angle galaxy bispectrum on the light-cone*, *Phys. Rev.* **D97** (2018), no. 2 023531, [[arXiv:1705.09306](#)].